An error-oriented Newton/inexact augmented Lagrangian approach for fully monolithic phase-field fracture propagation

Thomas Wick

Centre de Mathématiques Appliquées
École Polytechnique
Université Paris-Saclay
91128 Palaiseau, France

Accepted for publication in
SIAM Journal on Scientific Computing (SISC)
in March 2017

AN ERROR-ORIENTED NEWTON/INEXACT AUGMENTED LAGRANGIAN APPROACH FOR FULLY MONOLITHIC PHASE-FIELD FRACTURE PROPAGATION

THOMAS WICK*

Abstract. The purpose of this work is the development of a fully monolithic solution algorithm for quasi-static phase-field fracture propagation. Phase-field fracture consists of two coupled partial differential equations and it is well known that the underlying energy functional is non-convex and sophisticated algorithms are required. For the incremental, spatially-discretized problem, an adaptive error-oriented Newton algorithm is employed, which works as inner loop within an inexact augmented Lagrangian iteration. The latter approach relaxes the crack irreversibility constraint, which is an inequality constraint in time. Six numerical tests and benchmarks are consulted to demonstrate the performance of the algorithmic techniques. Specifically, the fully monolithic approach is compared to a quasi-monolithic approach in which phase-field is approximated through extrapolation in the displacement equation. These comparisons are done in terms of certain quantities of interest and computational cost. Moreover, features such as crack nucleation, joining, branching and fracture networks are addressed. Most examples are in 2D but 3D testing is provided as well. All findings are critically commented pointing to open questions and future improvements.

Key words. phase-field fracture propagation; error-oriented Newton method; inexact augmented Lagrangian; benchmark tests;

1. Introduction. Crack propagation is currently one of the major research topics in mechanical, energy, and environmental engineering. A popular variational approach for Griffith's [28] quasi-static brittle fracture has been introduced by Francfort and Marigo [24] (with according numerics presented in [14]), which has later been embedded into a thermodynamically-consistent phase-field technique by Miehe et al. [41].

Using such a variational approach, discontinuities in the displacement field u across the lower-dimensional crack surface are approximated by an auxiliary phase-field function φ. The latter can be viewed as an indicator function, which introduces a diffusive transition zone between the broken and the unbroken material. The essential aspects of a phase-field fracture propagation formulation are techniques that must include resolution of the length-scale parameter ε with respect to spatial discretization, the numerical solution of the forward problem and enforcement of the irreversibility of crack growth. The sum of these requirements leads to a variational inequality system in which we seek for the solution of $\{u, \varphi\}$.

A motivation for employing a phase-field model for fracture treatment is that crack nucleation, propagation, kinking, and curvilinear paths are automatically included in the model; post-processing of stress intensity factors and remeshing resolving the crack path become redundant. Furthermore, the underlying equations are based on continuum mechanics principles that can be treated with (adaptive) Galerkin finite elements. In fact, variational and phase-field formulations for fracture are active research areas as attested in recent years; see [14, 15, 38, 41, 32, 12, 7, 18, 1, 49, 3, 44, 45]. Recently, this basic model has been extended to pressurized fractures in elastic and porous media [42, 45, 53] and multiphysics fracture [39, 40, 37, 44, 43, 16, 29, 34, 35]. For a variational model for pressurized fractures and a sharp interface approximation, we refer to [2].

*Centre de Mathématiques Appliquées, École Polytechnique, Université Paris-Saclay, 91128 Palaiseau, France (thomas.wick@polytechnique.edu)

However, due to non-convexity of the underlying energy functional, in most approaches the solution is obtained via iteration between the variables [15, 13, 17, 36]. Such a partitioned approach might need many iterations; see [52, 25]. In addition, there are good reasons to aim for monolithic formulations such as numerical stability and consistent Galerkin formulations for gradient-based optimization [10] and dual-weighted a posteriori error estimation [11]. The latter topic in terms of phase-field fracture has been recently addressed in [56]. The key advantage of a monolithic formulation however is that the original system is solved without any modifications introduced by the numerical solution algorithm.

Consequently, the purpose of this paper is on monolithic techniques for quasi-static phase-field fracture. A robust computational framework in terms of a quasi-monolithic formulation has been proposed in [30]. Here, φ has been replaced in some terms by a linear extrapolation in time. However, a thorough theoretical justification is not available yet. In this paper, we compare this heuristic scheme with a fully monolithic formulation. For the latter one, a Newton method with standard (residual-based monotonicity) line-search will not work. Rather we employ an error-oriented Newton method [22], which is based on a natural monotonicity test rather than a residual-based criterion. We have no theoretical justification that this algorithm will always work well. Four benchmarks with different challenging properties indicate that the suggested methodology is robust. However, in a fifth example, the fully monolithic scheme with error-oriented criterion will not work, but only the quasi-monolithic approach. In the sixth example two 3D fractures are considered in a heterogeneous elastic medium. Our proposed technique has been further extended to couple dynamic (i.e., the solid equations include acceleration) pressurized phase-field fracture with fluid-structure interaction [55] in which also reasonable performance has been observed, and in particular the necessity to work with a modified Newton method allowing for an increase of the residual as the error-oriented method does.

Further algorithms for treating monolithic formulations have been recently suggested. Vignollet et al. [52] supplement the weak form with respect to a dissipation-based arc-length procedure in order to avoid a snapback behavior. Gerasimov and de Lorenzis [25] propose a line-search assisted Newton scheme. In both papers [52, 25] the authors also found that monolithic algorithms are computationally cheaper than partitioned algorithms. We finally notice that for dynamic phase-field fractures (i.e., not quasi-static) in pure elasticity (i.e., no crack pressure), monolithic schemes seem to work well without any modification of the Newton solver [12].

For crack irreversibility, we adopt a robust method from optimization: the augmented Lagrangian method dating back to Hestenes [31] and Powell [48] and proposed by Fortin and Glowinski [23] and Glowinski and le Tallec [27] for use in discretized differential equations. In terms of a partitioned phase-field fracture approach, this methodology has been successfully employed in [53].

In summary, the goals of this paper are:

- Formulating a fully monolithic displacement-phase-field fracture setting;
- Using a robust error-oriented Newton algorithm as adaptive inner solver inside an inexact augmented Lagrangian approach;
- Substantiating our algorithms for several benchmarks with various complexities.

To strengthen our findings, the error-oriented fully monolithic Newton approach will be compared to a classical residual-based Newton method for solving the quasi-monolithic formulation from [30].

The outline of this paper is as follows. In the first Section 2 the notation and the equations are provided. Next in Section 3 two Newton methods are explained. Then in Section 4, the Newton method serves as inner iteration within an inexact augmented Lagrangian penalization for the crack irreversibility constraint. Several benchmarks that include mechanics tests and pressurized fractures are consulted in Section 5 to substantiate our algorithmic developments. The paper is closed with concluding remarks in Section 6.

2. Notation and Governing Equations.

2.1. Notation. In this section, we introduce the basic notation and the underlying equations. In the following, let $B \subset \mathbb{R}^d, d = 2, 3$ the total domain wherein $\mathcal{C} \subset \mathbb{R}^{d-1}$ denotes the fracture and $\Omega \subset \mathbb{R}^d$ is the intact domain. We assume (possibly time-dependent non-homogeneous) Dirichlet conditions on the outer boundary ∂B.

Using a phase-field approach, the one-dimensional fracture $\mathcal{C}$ is approximated by $\Omega_F \in \mathbb{R}^d$ with the help of an elliptic (Ambrosio-Tortorelli) functional [4, 5]. For fracture formulations posed in a variational setting, this has been first proposed in [14]. The inner fracture boundary is denoted by $\partial\Omega_F$. The reader is referred to Figure 2.1 for an illustration of the notation. We emphasize that the domains B, Ω_F, and the boundary $\partial\Omega_F$ depend on the choice of the phase-field regularization parameter $\varepsilon > 0$. Finally, we denote the L^2 scalar product with $(\cdot, \cdot)$ as frequently used in the literature.

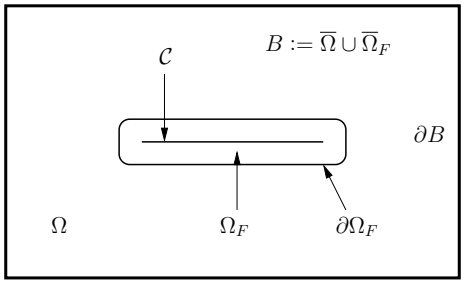

FIG. 2.1. *Setup of the notation: the unbroken domain is denoted by Ω and $\mathcal{C}$ is the fracture. The latter one is approximated by the domain Ω_F. The half thickness of Ω_F is ε. The fracture boundary is $\partial\Omega_F$ and the outer boundary is ∂B.*

2.2. Phase-field fracture. In this section, we recapitulate the ingredients for a phase-field model for mechanics and pressurized fractures in brittle materials. Such a model is based on the variational/phase-field fracture approach of [24, 14]. A thermodynamically-consistent phase-field technique using a stress-split into tension and compression has been proposed in [41].

The previous formulations start with an energy functional and the motion of the body under consideration is then determined by the Euler-Lagrange equations, which are obtained by differentiation with respect to the unknowns. Therefore, in phase-field-based fracture propagation, the unknown solution variables are vector-valued displacements $u : B \to \mathbb{R}^d$ and a smoothed scalar-valued indicator phase-field function $\varphi : B \to [0, 1]$. Here $\varphi = 0$ denotes the crack region and $\varphi = 1$ characterizes the unbroken material. The intermediate values constitute a smooth transition zone dependent on a regularization parameter ε. Adding a pressure $p : B \to \mathbb{R}$ to the Euler-Lagrange equations that acts on the fracture boundary has been formulated in [44, 45]. In all the previous fracture models, the physics of the underlying problem

ask to enforce a crack irreversibility condition (the crack can never heal) that is an inequality condition in time:

$$\partial_t \varphi \leq 0. \tag{2.1}$$

Consequently, modeling of fracture evolution problems leads to a variational inequality system, that is always, due to this constraint, quasi-stationary or time-dependent.

The resulting variational formulation is stated in an incremental (i.e., time-discretized) formulation in which the continuous irreversibility constraint is approximated by

$$\varphi \leq \varphi^{old}.$$

Here, φ^{old} will later denote the previous time step solution and φ the current solution. Let $V := H_0^1(B)$ and

$$W_{in} := \{w \in H^1(B) | \, w \leq \varphi^{old} \leq 1 \text{ a.e. on } B\}$$

be the function spaces we work with here; and for later purposes we also need $W := H^1(B)$. The Euler-Lagrange system for pressurized phase-field fracture reads [45]:

FORMULATION 1. *Let $p \in L^\infty(B)$ be given. Find vector-valued displacements and a scalar-valued phase-field variable $\{u, \varphi\} \in \{u_D + V\} \times W$ such that*

$$\begin{aligned} &\Big(\big((1-\kappa)\varphi^2 + \kappa\big)\, \sigma^+(u), e(w)\Big) + (\sigma^-(u), e(w)) \\ &\quad + (\varphi^2 p, div\ w) = 0 \quad \forall w \in V, \end{aligned} \tag{2.2}$$

and

$$\begin{aligned} &(1-\kappa)(\varphi\, \sigma^+(u) : e(u), \psi - \varphi) + 2(\varphi\, p\ div\ u, \psi - \varphi) \\ &+ G_c\Big(-\frac{1}{\varepsilon}(1-\varphi, \psi-\varphi) + \varepsilon(\nabla\varphi, \nabla(\psi-\varphi))\Big) \geq 0 \quad \forall \psi \in W_{in} \cap L^\infty(B). \end{aligned} \tag{2.3}$$

Here, G_c is the critical energy release rate, and we use the well-known law for the linear stress-strain relationship:

$$\sigma := \sigma(u) = 2\mu_s e(u) + \lambda_s \mathrm{tr} e(u) I, \tag{2.4}$$

where μ_s and λ_s denote the Lamé coefficients, $e(u) = \frac{1}{2}(\nabla u + \nabla u^T)$ is the linearized strain tensor and I is the identity matrix.

Furthermore in 2D, the stress σ is split into tensile σ^+ and compressive parts σ^- [38]:

$$\begin{aligned} \sigma^+ &= 2\mu_s e^+ + \lambda_s < \mathrm{tr}(e) > I, \\ \sigma^- &= 2\mu_s(e - e^+) + \lambda_s\big(\mathrm{tr}(e) - < \mathrm{tr}(e) >\big) I, \end{aligned}$$

and

$$e^+ = P \Lambda^+ P^T,$$

where $< \cdot >$ is the positive part of a function. Moreover, for $d = 2$, we have

$$\Lambda^+ := \Lambda^+(u) := \begin{pmatrix} < \lambda_1(u) > & 0 \\ 0 & < \lambda_2(u) > \end{pmatrix},$$

where $\lambda_1(u_{FM})$ and $\lambda_2(u_{FM})$ are the eigenvalues of the strain tensor e, and $v_1(u_{FM})$ and $v_2(u_{FM})$ the corresponding (normalized) eigenvectors. Finally, the matrix P is defined as $P := P(u_{FM}) := (v_1, v_2)$; namely, it consists of the column vectors $v_i, i = 1, 2$. In the 3D example we simply work in this paper with (2.4) because only tensile forces will occur in this specific test. Otherwise would have utilized the law proposed in [6] as we already implemented in our sister code [33]. A discussion of various laws can be found in [12][Section 2.2].

REMARK 2.1. *In Formulation 1, κ is a (small) positive regularization parameter for the elastic energy. Physically, κ represents the residual stiffness of the material. Consequently, since*

$$\big((1-\kappa)\varphi^2 + \kappa\big) \ \to \kappa \quad \textit{for } \varphi \to 0,$$

the material stiffness decreases while approaching the fracture zone.

REMARK 2.2. *The pressure terms $(\varphi^2 p, div\ w)$ and $2(\varphi\ p\ div\ u, \psi - \varphi)$ have been derived in [44, 45] and are based on an interface law that has been further manipulated using Gauss' divergence theorem.*

REMARK 2.3. *Formulation 1 does not explicitly contain time-derivatives. Rather, the time t might enter through time-dependent boundary conditions, e.g., $u_D = u_D(t) = g(t)$ on ∂B with a prescribed boundary function $g(t)$ of Dirichlet-type or through time-dependent right hand side forces, e.g., a time-dependent pressure force $p := p(t)$.*

REMARK 2.4. *Finally, we stress that Formulation 1 is nonlinear due to the monolithic formulation, the term $(1-\kappa)(\varphi\ \sigma^+(u) : e(u), \psi - \varphi)$, the stress splitting, and the inequality constraint.*

2.3. A linear-in-time extrapolation $\tilde{\varphi}$ in Equation (2.2). A well-known challenge in phase-field-based fracture formulations is related to the term

$$\big((1-\kappa)\varphi^2 + \kappa\big)\ \sigma^+(u).$$

The related energy term is not convex simultaneously in both solution variables u and φ, and requires sophisticated solution algorithms. In most cases, the solution is obtained via iteration between the variables [15, 13, 17, 36]. However such a partitioned approach might need many iterations. Therefore, and also for the sake of an accurate coupling, numerical stability and consistent Galerkin formulations for gradient-based optimization and dual-weighted a posteriori error estimation, monolithic approaches are in general preferable. One approach is based on a linear-in-time extrapolation of φ in Equation (2.2) in order to replace the $4th$-order non-convex term by a given coefficient in front of the elasticity. The extrapolated φ is denoted by $\tilde{\varphi}$ leading to

$$\big((1-\kappa)\tilde{\varphi}^2 + \kappa\big)\ \sigma^+(u)$$

in Formulation 1. On the one hand, this procedure is heuristic since in quasi-static fracture propagation, we cannot proof sufficient regularity in time; namely, the phase-field solution φ can have jumps in time. On the other hand, in [30], it has been numerically demonstrated that this procedure is robust. In terms of accuracy further numerical comparisons will be undertaken in the present paper.

2.4. Extrapolated quasi-monolithic and fully monolithic semi-linear forms. The final problem using the extrapolated $\tilde{\varphi}$ is stated in terms of a semi-linear form:

FORMULATION 2. *Find* $U := \{u, \varphi\} \in \{u_D + V\} \times W$ *such that*

$$\begin{aligned} A(U)(\Psi - U) = &\Big(\big((1-\kappa)\tilde{\varphi}^2 + \kappa\big)\ \sigma^+(u), e(w)\Big) + (\sigma^-(u), e(w)) + (\tilde{\varphi}^2 p, \nabla \cdot w) \\ &+ (1-\kappa)(\varphi\ \sigma^+(u) : e(u), \psi - \varphi) + 2(\varphi\ p\ \nabla \cdot u, \psi - \varphi) \\ &+ G_c\Big(-\frac{1}{\varepsilon}(1-\varphi, \psi - \varphi) + \varepsilon(\nabla\varphi, \nabla\psi - \nabla\varphi)\Big) \\ &\geq 0, \end{aligned} \tag{2.5}$$

for all $\Psi := \{w, \psi\} \in V \times W_{in}$. In order to deal with the variational inequality, the constraint $\varphi \leq \varphi^{old}$ is relaxed through penalization as it will be explained in Section 2.5.

REMARK 2.5 (A fully monolithic formulation). *A semi-linear form representing the fully monolithic formulation is obtained by replacing* $\tilde{\varphi}$ *by* φ *in Formulation 2.*

2.5. An incremental formulation using augmented Lagrangian penalization. Our strategy is as follows: we first discretize in time and work with the resulting incremental formulation. As already used in the definition of the space W_{in}, the irreversibility constraint (2.1) is discretized with a backward difference quotient such that

$$\frac{\varphi - \varphi^{n-1}}{\delta t} \leq 0,$$

where $\delta t = t^n - t^{n-1}$. Here, $\varphi^{n-1} := \varphi(t^{n-1})$ denotes the previous time step solution and $\varphi := \varphi^n := \varphi(t^n)$ the current solution. An augmented Lagrangian formulation of the irreversibility constraint reads:

$$\varphi \leq \varphi^{n-1} \quad \rightarrow \quad \Big[\Xi + \gamma(\varphi - \varphi^{n-1})\Big]^+$$

where $\Xi \in L^2$ and $\gamma > 0$ and $[x]^+ := max(x, 0)$. The resulting formulation then reads:

FORMULATION 3. *Find* $U = \{u, \varphi\} \in \{u_D + V\} \times W$ *such that*

$$A(U)(\Psi) := \tilde{A}(U)(\Psi) + [\Xi + \gamma(\varphi - \varphi^{n-1})]^+ = 0 \quad \forall \Psi \in V \times W,$$

where

$$\begin{aligned} \tilde{A}(U)(\Psi) = &\Big(\big((1-\kappa)\tilde{\varphi}^2 + \kappa\big)\ \sigma^+(u), e(w)\Big) + (\sigma^-(u), e(w)) + (\tilde{\varphi}^2 p, \nabla \cdot w) \\ &+ (1-\kappa)(\varphi\ \sigma^+(u) : e(u), \psi) + 2(\varphi\ p\ \nabla \cdot u, \psi) \\ &+ G_c\Big(-\frac{1}{\varepsilon}(1-\varphi, \psi) + \varepsilon(\nabla\varphi, \nabla\psi)\Big). \end{aligned} \tag{2.6}$$

REMARK 2.6. *The penalization function* Ξ *is computed as usually by an additional iteration. Details are provided in Section 4.*

REMARK 2.7 (A fully monolithic form). *The corresponding fully monolithic form to* (2.6) *is again obtained by replacing* $\tilde{\varphi}$ *by* φ.

3. Residual-based and error-oriented Newton methods. One goal of this paper is to get rid of the extrapolation of Section 2.3 with the reasons outlined therein. The key methodology to deal with a fully monolithic formulation lies in appropriate modifications of Newton's method for solving the nonlinear problem. One possibility in terms of a line-search assisted Newton method has been recently proposed in [25]. In this paper, we employ an error-oriented Newton algorithm as outlined in [22]. This method can specifically cope with highly nonlinear problems and the key feature of this algorithm is that it is based on a natural monotonicity test in which the ordinary Newton update is compared to a simplified Newton update. For better comparisons, we additionally employ a classical residual-based Newton method with a standard backtracking line search. We begin this section with the spatial discretization.

3.1. Spatial discretization. The previous equations are spatially discretized with a Galerkin finite element scheme, introducing H^1 conforming discrete spaces $V_h \subset V$ and $W_h \subset W$ consisting of bilinear functions Q_1^c on quadrilaterals. The discretization parameter is denoted by h. The discretized version of Formulation 3 (respectively Remark 2.7) reads:

FORMULATION 4. *Find* $U_h = \{u_h, \varphi_h\} \in \{u_D^h + V_h\} \times W_h$ *such that*

$$A(U_h)(\Psi_h) := \tilde{A}(U_h)(\Psi_h) + [\Xi_h + \gamma(\varphi_h - \varphi_h^{n-1})]^+ = 0 \quad \forall \Psi \in V_h \times W_h.$$

In the following we however omit the index h to simplify the notation.

3.2. The Jacobian matrix. For both Newton methods we construct the Jacobian by evaluating the directional derivative $A'(U)(\delta U, \Psi)$ with the Newton update $\delta U := \{\delta u, \delta\varphi\} \in V \times W$. In detail the extrapolated version reads:

$$\begin{aligned}
&A'(U)(\delta U, \Psi)\\
&= \Big(\big((1-\kappa)\tilde{\varphi}^2 + \kappa\big)\ \sigma^+(\delta u), e(w)\Big) + (\sigma^-(\delta u), e(w))\\
&\quad + (1-\kappa)(\delta\varphi\sigma^+(u) : e(u) + 2\varphi\ \sigma^+(\delta u) : e(u), \psi) + 2p(\delta\varphi\nabla\cdot u + \varphi\ \nabla\cdot\delta u, \psi)\\
&\quad + G_c\Big(\frac{1}{\varepsilon}(\delta\varphi, \psi) + \varepsilon(\nabla\delta\varphi, \nabla\psi)\Big)\\
&\quad + \gamma(\delta\varphi, \psi)_{A(\varphi)} \quad \forall \Psi := \{w, \psi\} \in V \times W,
\end{aligned} \tag{3.1}$$

and the fully monolithic version is given by:

$$\begin{aligned}
&A'(U)(\delta U, \Psi)\\
&= \Big(2\delta\varphi(1-\kappa)\varphi\sigma^+(u) + \big((1-\kappa)\varphi^2 + \kappa\big)\ \sigma^+(\delta u), e(w)\Big) + (\sigma^-(\delta u), e(w))\\
&\quad + 2\,(\delta\varphi\,\varphi p, \mathrm{div}\ w)\\
&\quad + (1-\kappa)(\delta\varphi\sigma^+(u) : e(u) + 2\varphi\ \sigma^+(\delta u) : e(u), \psi) + 2p(\delta\varphi\nabla\cdot u + \varphi\ \nabla\cdot\delta u, \psi)\\
&\quad + G_c\Big(\frac{1}{\varepsilon}(\delta\varphi, \psi) + \varepsilon(\nabla\delta\varphi, \nabla\psi)\Big)\\
&\quad + \gamma(\delta\varphi, \psi)_{A(\varphi)} \quad \forall \Psi := \{w, \psi\} \in V \times W,
\end{aligned} \tag{3.2}$$

where

$$\mathcal{A}(\varphi) = \{x = (x_1, x_2) \in B \,|\, \gamma(\varphi(x) - \varphi(x)^{n-1}) > 0\}.$$

In $\sigma^+(\delta u)$ and $\sigma^-(\delta u)$ we employ the derivative of e^+, which is given by

$$e^+(\delta u) = P(\delta u)\Lambda^+ P^T + P\Lambda^+(\delta u)P^T + P\Lambda^+ P^T(\delta u).$$

3.3. Residual-based Newton's method with line-search and quasi-Newton steps. In this section, we recapitulate a classical Newton algorithm. Globalization is achieved by a damping strategy based on a line search algorithm. However, in contrast to [25] (who managed to design a sophisticated line-search procedure), our line search strategy is kept simple based on monotonicity-based backtracking. Unfortunately, such a procedure turns out to be too simple and does not converge using a fully monolithic procedure. In [30] it has been however shown that this method is efficient and robust when the convexification trick, see Section 2.3, based on linear-in-time extrapolation for φ is adopted. To measure the residuals and monitoring functions, we use the discrete norm $\|\cdot\| := \|\cdot\|_{l^2}$.

ALGORITHM 3.1 (Residual-based Newton's method). *In this type of methods, the main criterion is a decrease of the residual in each step. Choose an initial Newton guess U^0. For the iteration steps $k = 1, 2, 3, \ldots$:*

1. *Find $\delta U^k := \{\delta u, \delta\varphi\} \in V \times W$ such that*

$$A'(U^k)(\delta U^k, \Psi) = -A(U^k)(\Psi) \quad \forall \Psi \in V \times W,$$
$$U^{k+1} = U^k + \lambda_k \delta U^k,$$

   for $\lambda_k = 1$.
2. *The criterion for convergence is contractions of the residuals:*

$$\|A(U^{k+1})(\Psi)\| < \|A(U^k)(\Psi)\|. \tag{3.3}$$

3. *If (3.3) is violated, replace U^{k+1} by choosing $\lambda_k^l = 0.5$, and computing for $l = 1, ..., l_M$ (e.g. $l_M = 20$) a new solution*

$$U^{k+1} = U^k + \lambda_k^l \delta U^k$$

   until (3.3) is fulfilled for a $l^* < l_M$ or l_M is reached. In the latter case, no convergence is obtained and the program aborts.
4. *In case of $l^* < l_M$ we check next the stopping criterion:*

$$\|A(U^{k+1})(\Psi)\| \leq TOL_N.$$

   If this is criterion is fulfilled, set $U^* := U^{k+1}$. Else, we increment $k \to k+1$ and goto Step 1.

REMARK 3.1 (Quasi-Newton steps). *In order to accelerate Newton's method close to the solution U^* we use intermediate quasi-Newton steps. In the case of $\lambda_k = 1$ we monitor*

$$\theta_k = \frac{\|A(U^{k+1})(\Psi)\|}{\|A(U^k)(\Psi)\|}.$$

If $\theta_k \leq \theta_{max} < 1$ (where e.g. $\theta_{max} \approx 0.1$), then we do not build the Jacobian and use the last version that is available.

3.4. An error-oriented Newton method. In order to cope with the fully monolithic Formulation 4 (replacing therein $\tilde{\varphi}$ by φ), we adopt an error-oriented Newton solver as it has been suggested in [22]. This approach yields a higher robustness at the time point when the fracture starts growing. As before, to measure the residuals and monitoring functions, we use the discrete norm $\|\cdot\| := \|\cdot\|_{l^2}$.

The details of this algorithm are as follows:

ALGORITHM 3.2 (Error-oriented Newton's method). *The main criterion of this method is based on a decrease of the norm of the update δU^k. Set $\lambda_{min} \sim 10^{-10}$. Choose an initial Newton guess U^0. For $k = 1, 2, 3, \ldots$:*

1. *Solve for* $\delta U^k := \{\delta u, \delta\varphi\} \in V \times W$*:*

$$A'(U^k)(\delta U^k, \Psi) = -A(U^k)(\Psi) \quad \forall \Psi \in V \times W.$$

2. *Check if* $\|\delta U^k\| \leq TOL_N$*. If true, the solution is found and set*

$$U^* := U^k + \delta U^k.$$

Else and if $k > 0$ *compute a prediction value for the damping factor:*

$$\lambda_k := \min(1, \mu_k), \quad \mu_k := \frac{\|\delta U^{k-1}\| \cdot \|\delta U^k_{simp}\|}{\|\delta U^k_{simp} - \delta U^k\| \cdot \|\delta U^k\|},$$

where δU^k_{simp} *is available from the previous iteration* $k-1$ *by solving the simplified system* (3.6)*.*

3. *If*

$$\lambda_k < \lambda_{min} \tag{3.4}$$

then terminate the program due to convergence failure.

4. *If* $\lambda_k > \lambda_{min}$ *continue and compute the trial iterate*

$$U^{k+1} := U^k + \lambda_k \delta U^n \tag{3.5}$$

and evaluate the new residual $A(U^{k+1})(\Psi)$*. Solve the simplified linear system using the old Jacobian: Find* $\delta U^{k+1}_{simp} := \{\delta u_{simp}, \delta\varphi_{simp}\} \in V \times W$*:*

$$A'(U^k)(\delta U^{k+1}_{simp}, \Psi) = -A(U^{k+1})(\Psi) \quad \forall \Psi \in V \times W. \tag{3.6}$$

5. *Compute the monitoring functions:*

$$\theta_k := \frac{\|\delta U^{k+1}_{simp}\|}{\|\delta U^k\|}, \quad \mu'_k := \frac{0.5\|\delta U^k\| \cdot \lambda_k^2}{\|\delta U^{k+1}_{simp} - (1-\lambda_k)\delta U^k\|}, \quad \lambda'_k := \min(\mu'_k, \frac{1}{2}\lambda_k)$$

6. *If* $\theta_k \geq 1$ *(no convergence of the updates) set*

$$\lambda_k := \lambda'_k$$

and go to Step 3 and continue from there.

7. *If* $\theta_k < 1$*, we have convergence and continue:*
   (a) *If* $\lambda'_k = \lambda_k = 1$*, check if*

$$\|\delta U^{k+1}_{simp}\| \leq TOL_N$$

then stop and the solution is found:

$$U^* := U^{k+1} + \delta U^{k+1}_{simp}.$$

   (b) *Else accept* U^{k+1} *(computed in* (3.5)*) as new iterate. Then increment* $k \to k+1$ *and goto to the beginning to Step 1.*

REMARK 3.2. *Within Newton's method the linear equation systems are solved with the direct solver UMFPACK [20].*

4. An inexact augmented Lagrangian/error-oriented Newton approach. In the previous section, our focus has been on solving the forward model while tacitly assuming that the inequality constraint is taken care of. In order to enforce this constraint, we employ an augmented Lagrangian loop. At each time $t^n, n \in \mathbb{N}$, the augmented Lagrangian loop constitutes the outer loop wherein at each step the Newton solver is adopted. Moreover, we propose an (heuristic) adaptive criterion in order to reduce the computational cost. This leads to an inexact augmented Lagrangian/error-oriented Newton loop.

4.1. Augmented Lagrangian penalization. The iteration reads:

ALGORITHM 4.1 (Augmented Lagrangian loop with error-oriented Newton). *At each $t^n, n = 0, 1, 2, \ldots$ let $\Xi_{h,0}$ be given, e.g., $\Xi_{h,0} = 0$. Moreover, let $\gamma > 0$ be fixed and given for all t^n. At each time t^n iterate for $m = 0, 1, 2, \ldots$*

1. *Given $\Xi_{h,m}$, we seek $U^n_{h,m+1} = \{u^n_{h,m+1}, \varphi^n_{h,m+1}\}$ by solving Formulation 4 with Newton's method via Algorithm 3.2.*
2. *Update*

$$\Xi_{h,m+1} = [\Xi_{h,m} + \gamma(\varphi_{h,m+1} - \varphi_h^{n-1})]^+.$$

3. *Check the stopping criterion*

$$\{\|u^n_{h,m+1} - u^n_{h,m}\|_{L^2}, \|\Xi_{h,m+1} - \Xi_{h,m}\|_{L^2}\} \leq \mathrm{TOL}_{\mathrm{AL}}, \quad \mathrm{TOL}_{\mathrm{AL}} > 0. \quad (4.1)$$

4. *a) If the stopping criterion is satisfied, set $U^n_h := U^n_{h,m^*}$ where m^* is the m that satisfies* (4.1).
   b) Else increment $m \to m + 1$ and go to Step 1.

REMARK 4.1. *Algorithm 4.1 works in the exact same fashion by replacing the error-oriented Newton algorithm by the residual-based version. However as previously motivated, the residual-based version only works well with the quasi-monolithic formulation in which φ is extrapolated.*

4.2. An adaptive Newton stopping criterion for an inexact augmented Lagrangian method. In order to decrease the computational cost, we adaptively determine the stopping tolerance of Newton's method depending on the augmented Lagrangian norm. Such strategies are in particular well-known for (adaptive) inexact Newton methods, e.g., [21, 19, 22], in which the linear equations are only approximatively solved at each stage. Related techniques using adaptive (or inexact) augmented Lagrangian realizations are discussed, for instance, in [47]. In all these adaptive inexact methods, the accuracy of the inner method should be chosen as such that the convergence pattern of the outer loop remains unperturbed.

PROPOSITION 4.2. *For $m = 0$ set $\Xi_{h,0}$ and, e.g., $TOL_N = 10^{-8}$. For $m = 1, 2, 3, \ldots$ use Algorithm 4.1 and compute in Step 4b*

$$\Delta := \|\Xi_{h,m+1} - \Xi_{h,m}\|_{L^2}.$$

For each further augmented Lagrangian step m, we use in the inner Newton loop (part of Step 1) as stopping criterion

$$TOL_N := \alpha\Delta,$$

where $\alpha = 10^{-3} < 1$. The most important question in this respect is what level of accuracy of the inner solver (here Newton's method) is required to preserve convergence

of the outer loop. As it is well-known the inner loop must be solved with a higher accuracy than the outer loop, i.e., $TOL_N < TOL_{AL}$. Therefore, $\alpha < 1$ is a necessary choice. From our practical observations in this paper, the largest α should be chosen as 10^{-3} in these types of problems.

5. Numerical tests. In this final section, we consult six scenarios that include a benchmark from mechanics, e.g., [38], a second mechanics test with cyclic loading [3], a pressurized stationary crack (Sneddon) in which only the crack width varies [51], and a propagating pressurized fracture [53]. In test 5, another engineering example in form of a screw tension test is considered [54] in which cracks will nucleate due to high pressure and secondly a hollow-rolled screw will create a fracture network. In the final test, a 3D setting in a heterogeneous medium is considered. In all tests quantitative comparisons to the extrapolated scheme from [30] are undertaken. For the sake of fair comparisons, only uniform mesh refinement is adopted in the first five tests and pre-defined local mesh refinement in the sixth test. Augmenting the current schemes with a posteriori-based mesh adaptivity requires some work but is in principle straightforward as shown for related problems using residual-based a posteriori error estimation [17, 18, 7], goal-oriented dual-weighted residual mesh refinement [56] or predictor-corrector mesh adaptivity [30] (2D) and in 3D [33]. All numerical examples in this paper are computed with a self-developed code based on the finite element package deal.II [9, 8].

5.1. Single edge notched shear test. In this first example, we restrict our attention to pure elastic crack-propagation examples in order to test our solver for cases with unstable and brutal crack growth. The geometric and material properties are the same as used in [38]. In the single edge notched shear test, it is important to consider the correct boundary conditions and the spectral decomposition of the stress $\sigma(u)$ into tensile $\sigma^+(u)$ and compressive parts $\sigma^-(u)$. We refer to [41, 6] for a detailed physical motivation.

Configuration. The geometry and boundary conditions are displayed in Figure 5.1. In particular the initial domain has already a slit (fracture). The initial mesh is $4, 5$ and 6 times uniformly refined, leading to $1024, 12771$ and 50115 mesh cells, with $h = 0.044mm, 0.022mm$ and $0.011mm$, respectively.

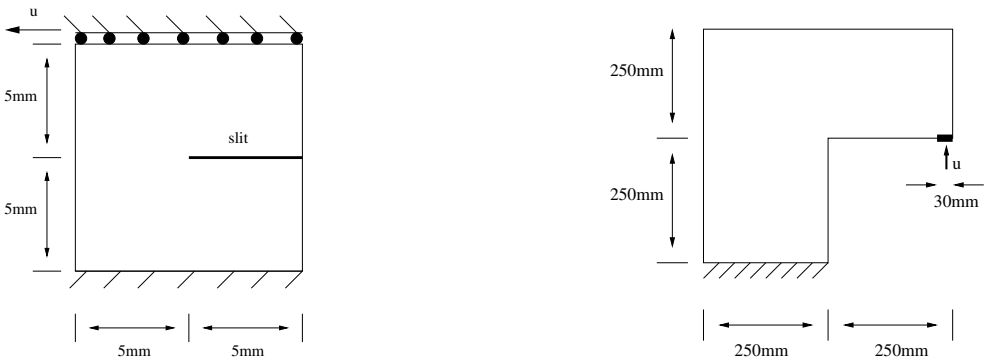

FIG. 5.1. *Example 1 and 2: Single edge notched shear test (left) and L-shaped panel test (right). We prescribe the following conditions: On the left and right boundaries, $u_y = 0mm$ and traction-free in x-direction. On the bottom part, we use $u_x = u_y = 0mm$ and on Γ_{top}, we prescribe $u_y = 0mm$ and u_x as stated in* (5.1)*. Finally, the lower part of the slit is fixed in y-direction, i.e., $u_y = 0mm$. For the L-shaped panel test (at right), the lower left boundary is fixed: $u_x = u_y = 0$. A displacement condition for u_y is prescribed by* (5.2) *in the right corner on a section Γ_u that has $30mm$ length.*

Boundary conditions. We increase the displacement on Γ_{top} over time, namely we apply a time-dependent non-homogeneous Dirichlet condition:

$$u_x = t\bar{u}, \quad \bar{u} = 1 \text{ mm/s}, \tag{5.1}$$

where t denotes the total time.

Parameters. Specifically, we use $\mu = 80.77kN/mm^2$, $\lambda = 121.15kN/mm^2$, and $G_c = 2.7N/mm$. In this example $p = 0$. The time step size is chosen as $\delta t = 10^{-4}s$. The tolerance of the augmented Lagrangian loop is $TOL_{AL} = 10^{-4}$. Furthermore, we set $k = 10^{-10}h[mm]$ and $\varepsilon = 2h$ (Case 1) and $\varepsilon = h_{coarse} = 0.8844mm$ (Case 2), respectively. If not otherwise denoted we consider as 'standard' test in this example Case 1.

Quantities of interest. We evaluate the surface load vector on $\Gamma_{top} := \{(x, y) \in B | \, 0mm \leq x \leq 10mm, \, y = 10mm\}$ as

$$\tau = (F_x, F_y) := \int_{\Gamma_{top}} \sigma(u) n \, ds,$$

with normal vector n, and we are particularly interested in F_x. Moreover, we observe the number of Newton steps and compare the fully monolithic formulation with the extrapolation-in-time.

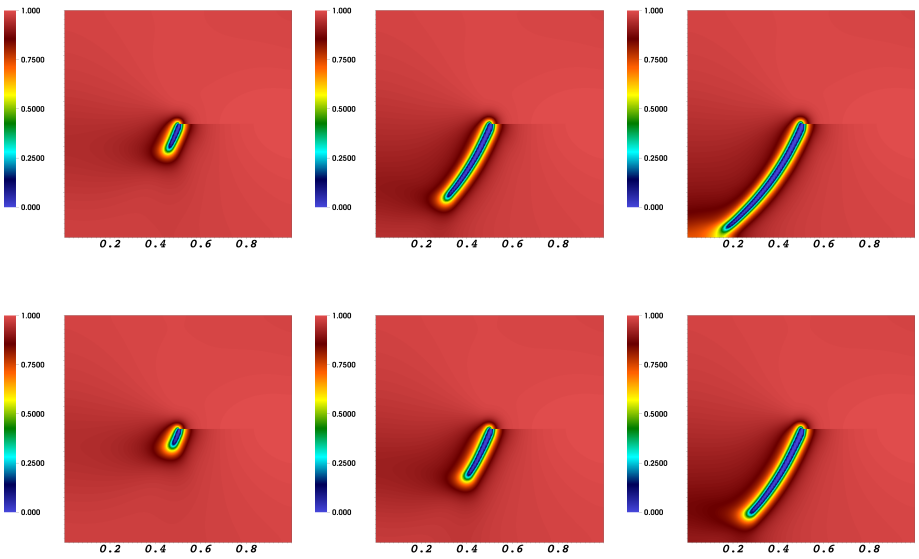

FIG. 5.2. *Example 1: Single edge notched shear test. Display of the phase-field function at* $T = 0.0105s, 0.012s$ *and* $T = 0.013s$. *We observe that the crack grows slower using the extrapolated scheme.*

Discussion of findings. Numerical solutions of the crack pattern (i.e., the phase-field variable) are displayed in Figure 5.2. The surface load evolution is plotted in Figure 5.3. Finally, the number of Newton iterations is shown in Figure 5.4. Up to time step 95 the number of Newton iterations is between 4 and 10 per time step. Once the fracture starts growing we observe an increase of Newton steps for certain time

steps, specifically using the fully monolithic scheme. This behavior is in agreement with the observations made in [25]. We remark that in most tests no augmented Lagrangian iterations have been required in order to reach the tolerances. In two monolithic tests, Case 1, Ref. 5 and Case 2, Ref. 6, TOL_{AL} has not been immediately achieved but after 4 and 2 augmented Lagrangian iterations, respectively. In these two tests, the initial Newton convergence was poor but significantly improved after updating Ξ. Thus, for these two cases, we notice 43 and 39 respective Newton iterations as it can be monitored in Figure 5.4.

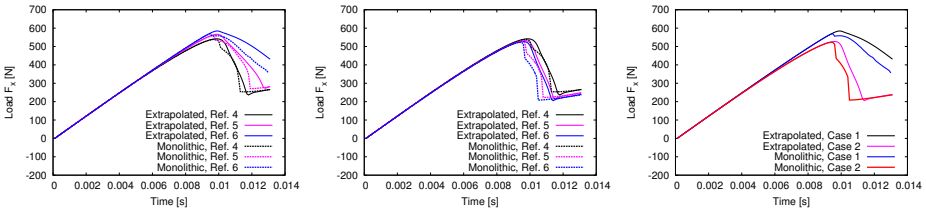

FIG. 5.3. *Example 1: Load displacement curves for Case 1 (left), Case 2 (middle), and a comparison of Case 1 and 2 on the refinement level 6 (right). We monitor that Case 1 yields no convergence. This is in agreement with observations made in [30]. Fixing $\varepsilon = 0.0884mm$, yields clearly convergence under h-refinement as plotted in the middle figure. The right figure highlights the differences using the extrapolated vs. the monolithic scheme on the finest mesh level.*

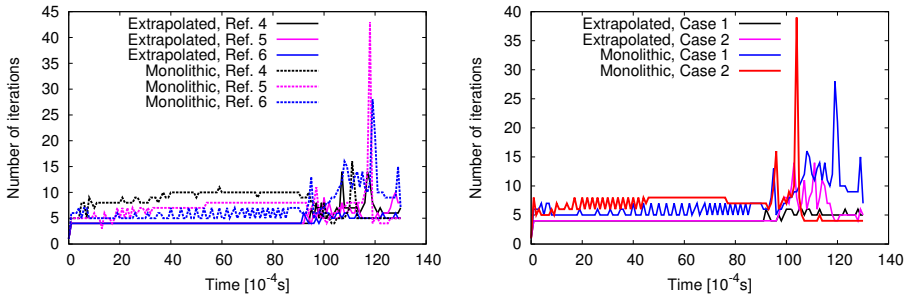

FIG. 5.4. *Example 1: Number of Newton iterations per time step. At left, the iterations for the extrapolated scheme and the monolithic scheme for Case 1 are shown. On the right, the results for the Cases 1/2 on the finest mesh level Ref. 6 are displayed.*

5.2. L-shaped panel test. In this second example, we consult another well-known test from mechanics. An experimental set-up is described in [57]. Numerical simulations using variational/phase-field type approaches are reported in [3, 36, 25].

Configuration. The geometry and boundary conditions are displayed in Figure 5.1. In contrast to the first example, no initial crack is prescribed. The initial mesh is $2, 3, 4$ and 5 times uniformly refined, leading to $1200, 4800, 19200$ and 76800 mesh cells, with $h = 14.577mm, 7.289mm, 3.644mm$ and $1.822mm$, respectively.

Boundary conditions. We increase the displacement $u_D := u_y = u_y(t)$ on $\Gamma_u := \{(x, y) \in B | \, 470mm \leq x \leq 500mm, \, y = 250mm\}$ over time, where Γ_u is a section of $30mm$ length on the right corner of the specimen. We apply a time-dependent

non-homogeneous Dirichlet condition [3]:

$$\begin{aligned} u_y &= t \cdot \bar{u}, & \bar{u} &= 1 \text{ mm/s}, & 0.0s \leq t < 0.3s, \\ u_y &= (0.6 - t) \cdot \bar{u}, & \bar{u} &= 1 \text{ mm/s}, & 0.3s \leq t < 0.8s, \\ u_y &= (-1 + t) \cdot \bar{u}, & \bar{u} &= 1 \text{ mm/s}, & 0.8s \leq t \leq 2.0s, \end{aligned} \tag{5.2}$$

where t denotes the total time. Due to this cyclic loading the total displacement at the end time $T = 2s$ is $1mm$.

Parameters. We use $\mu = 10.95kN/mm^2$, $\lambda = 6.16kN/mm^2$, and $G_c = 8.9 \times 10^{-5}kN/mm$. In this example $p = 0$. The time step size is $\delta t = 10^{-3}s$. Furthermore, we set $k = 10^{-10}h[mm]$ and $\varepsilon = 2h$. Finally, $TOL_{AL} = 10^{-4}$.

Quantities of interest. As before, we observe the number of Newton iterations and we evaluate the surface load vector on $\Gamma_{top} := \{(x, y) \in B | \, 0mm \leq x \leq 500mm, \, y = 500mm\}$ as

$$\tau = (F_x, F_y) := \int_{\Gamma_{top}} \sigma(u) n \, ds,$$

with normal vector n, and now we are particularly interested in F_y.

Discussion of findings. In Figure 5.5 the crack path in terms of the phase-field variable is shown. Next, in Figure 5.6, the load-displacement curves are displayed. These findings are in good agreement with [3]. Under mesh refinement, convergence of this goal-functional is shown. That the load significantly decreases under mesh refinement has been confirmed in [26]. In contrast to Example 1, Section 5.1, there is no significant difference between the extrapolated model and the fully monolithic approach. Moreover, the number of Newton steps is reasonable throughout the entire simulation as shown in Figure 5.6. In order to solve the system per time step, no augmented Lagrangian iterations are required (thus a plot is omitted).

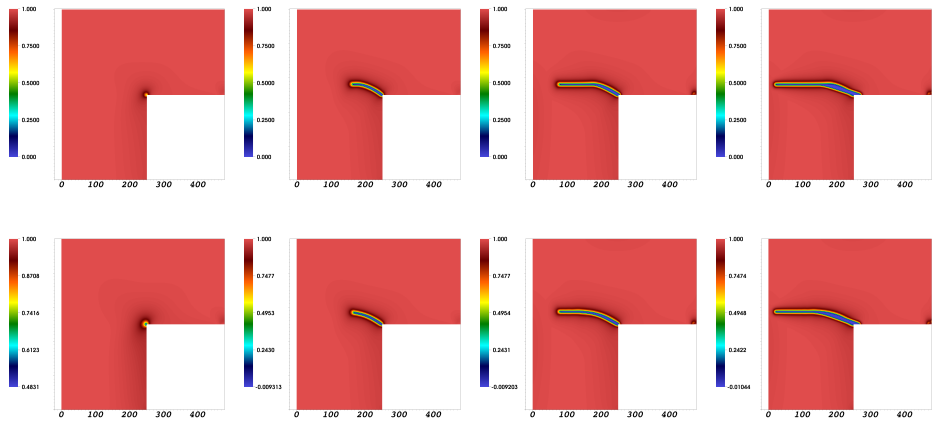

FIG. 5.5. *Example 2: L-shaped panel test. Display of the phase-field function for* $u_y|_{\Gamma_u} = 0.22mm, 0.3mm, 0.45mm, 1mm$. *These qualitative results are in excellent agreement with [3]. Furthermore, no differences in the crack path between the fully monolithic (top row) and the extrapolated scheme (bottom row) can be detected.*

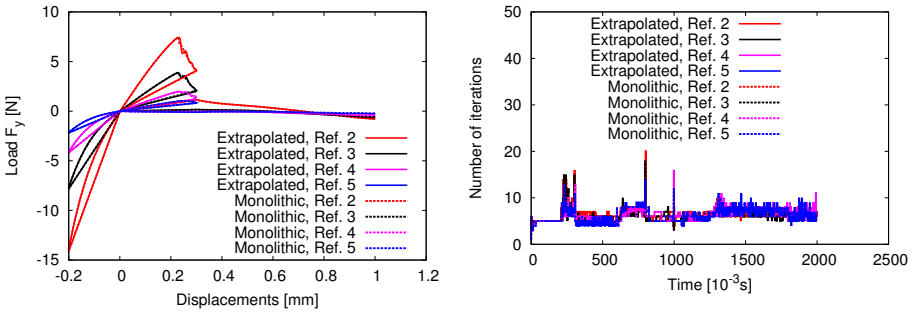

FIG. 5.6. *Example 2: Load-displacement curve (at left) and the number of Newton iterations per loading step (at right).*

5.3. A stationary pressurized fracture (Sneddon). This example is based on the theoretical calculations of [51, 50]. A (constant) pressure $p = 10^{-3}Pa$ causes the fracture to change its width but is low enough to change the length.

Configuration. We deal with the following geometric data: $\Omega = (0m, 4m)^2$ and a (prescribed) initial crack with half length $l_0 = 0.2m$ on $\Omega_F = (1.8-h, 2.2+h) \times (2-h, 2+h) \subset \Omega$. This initial crack is given with the help of the phase-field function φ. We set at $t = 0$:

$$\varphi = 0 \quad \text{in } \Omega_F, \quad \text{and} \quad \varphi = 1 \quad \text{in } B \setminus \Omega_F. \tag{5.3}$$

As boundary conditions, we set the displacements to zero on $\partial\Omega$. The initial mesh is $6, 7$ and 8 times uniformly refined, leading to $4096, 16384$ and 65536 mesh cells, with $h = 0.088m, 0.044m$ and $0.022m$, respectively.

Parameters. The fracture toughness is chosen as $G_c = 1.0N/m$. The mechanical parameters are Young's modulus and Poisson's ratio $E_s = 1.0Pa$ and $\nu_s = 0.2$. The relationship to the Lamé coefficients μ_s and λ_s is given by:

$$\mu_s = \frac{E_s}{2(1+\nu_s)}, \qquad \lambda_s = \frac{\nu_s E_s}{(1+\nu_s)(1-2\nu_s)}.$$

The regularization parameters are chosen as $\varepsilon = 2h$ and $\kappa = 10^{-10}h$. Furthermore, $TOL_{AL} = 10^{-3}$. This test case is computed in a quasi-stationary manner, which is due to the crack irreversibility constraint. That is, we solve 5 pseudo-time steps until the residual error is sufficiently small.

Quantities of interest.

- The crack opening displacement (COD; also known as aperture) for both the extrapolated scheme and the fully monolithic technique:

$$COD = \int_0^4 u(x_0, y) \cdot \nabla\varphi(x_0, y)\, dy, \tag{5.4}$$

  where φ is as before our phase-field function and x_0 the x-coordinate of the integration line. The analytical solution for the crack opening displacement derived by Sneddon and Lowengrub [51] is given by:

$$COD = 2\frac{pl_0}{E'}\big(1 - \frac{x^2}{l_0^2}\big)^{1/2} = 3.84 \times 10^{-4}\big(1 - \frac{x^2}{l_0^2}\big)^{1/2},$$

  where $E' = \frac{E_s}{1-\nu_s^2}$;

- The number of augmented Lagrangian steps per pseudo time-step until TOL_{AL} is achieved;
- The number of total Newton steps per pseudo time-step.

Discussion of findings. Our findings are displayed in the Figures 5.7, 5.8, and 5.9. As in Example 2, Section 5.2, we do not observe significant differences between the extrapolated and the fully monolithic scheme. In contrast to the previous examples, the penalization is now active and several augmented Lagrangian steps are required to satisfy TOL_{AL}. Here however, differences are only observed with respect to the mesh level but not to the scheme (extrapolated or monolithic). The accumulated number of Newton steps per (pseudo) time step is very reasonable and is of about 25 to 50 iterations; except for the initial step since the initial displacement solution (which is zero) is far away from the final state.

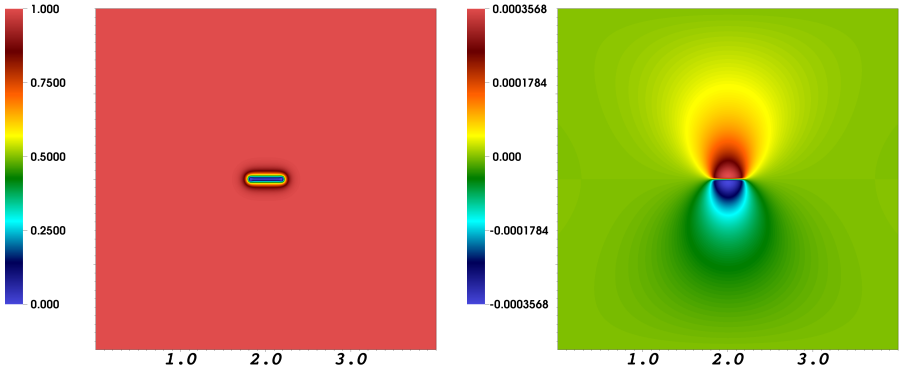

FIG. 5.7. *Example 3: Sneddon's test. Phase-field function (left) and u_y-displacements. Since the fracture is parallel to the x-axis, the u_y-displacements represent the COD in this example.*

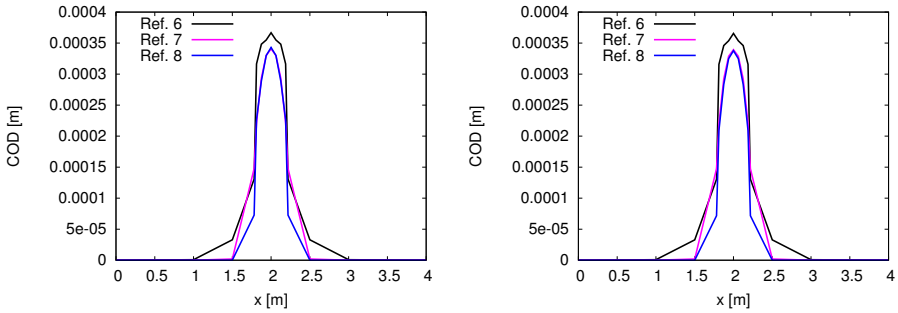

FIG. 5.8. *Example 3: Crack opening displacement using the extrapolated scheme (left) and the fully monolithic approach (right).*

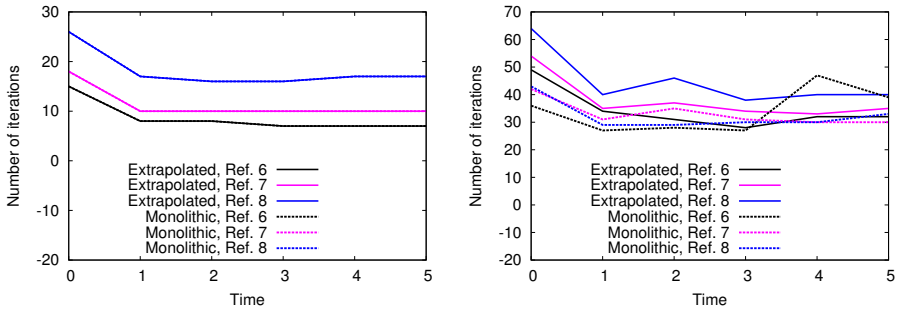

FIG. 5.9. *Example 3: Number of iterations per time step of the augmented Lagrangian loop (left) and the accumulated number of Newton iterations (at right).*

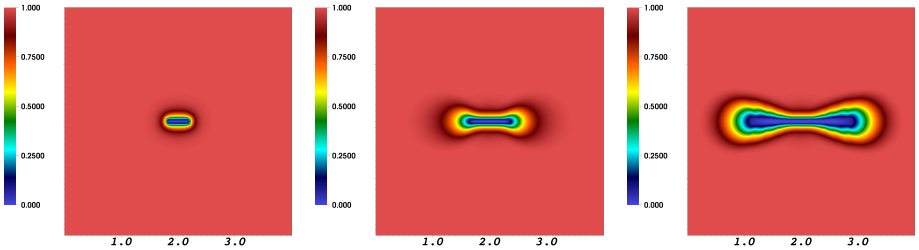

FIG. 5.10. *Example 4: Phase-field function using the extrapolated scheme for pressure values* $p = 0.0, 1.60, 1.90Pa$.

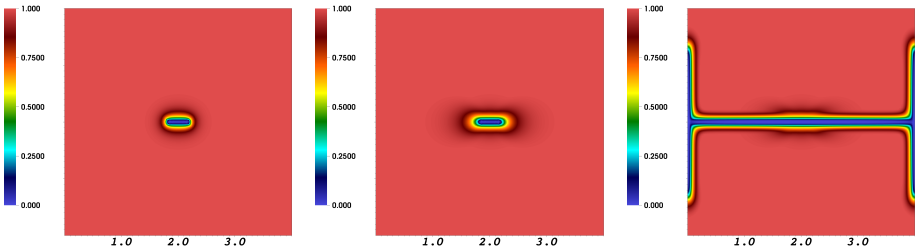

FIG. 5.11. *Example 4: Phase-field function using the monolithic scheme for pressure values* $p = 0.0, 1.24, 1.25Pa$.

5.4. A propagating pressurized fracture. In this fourth test, we consider a pressurized propagating fracture. The configuration is the same as presented in [53] and more specifically the geometry and all parameters (except the pressure) are provided in Example 3, Section 5.3. At each time step the pressure load p is increased. Using the extrapolated scheme we prescribe:

$$p(t) = 0.1 + t \cdot 0.1, \qquad 0s \leq t \leq 19s,$$

where t denotes the current time. It turns out that this increase is too strong for the fully monolithic coupling and there we use:

$$p(t) = \begin{cases} 0.1 + 0.1t, & 0s \leq t \leq 11s, \\ 1.2 + 0.01(t - 11), & 12s \leq t \leq 16s. \end{cases}$$

The simulation is performed on the finest mesh level $h = 0.011m$. In fact, this example is a very hard test since unstable brutal crack growth occurs.

Quantities of interest. We observe the length of the fracture as well as the number of iterations.

Discussion of findings. In contrast to the other examples, we observe a dramatic difference between the extrapolated scheme and the fully monolithic scheme as illustrated in the Figures 5.10 and 5.11. In fact using the monolithic scheme the crack suddenly damages the entire domain. For better comparison in Figure 5.12, the fracture length is also compared to the partitioned scheme from [53]. The number of Newton steps becomes very high once the fracture starts propagating. Careful inspection of this example leads us to the conclusion that the suggested Newton solver for pressurized fractures with fast crack growth might be further refined in future research. We refer exemplarily to the optimization literature [46] for possible further improvements of Newton's method. Unfortunately this example demonstrates in a very illustrative way that crack growth might highly depend on the solution algorithm. The partitioned scheme and the extrapolated scheme relax the applied forces and lead to a slower crack growth than the monolithic scheme. On the other hand this result confirms one purpose of this paper; namely that monolithic schemes better account for the accuracy of the coupling conditions.

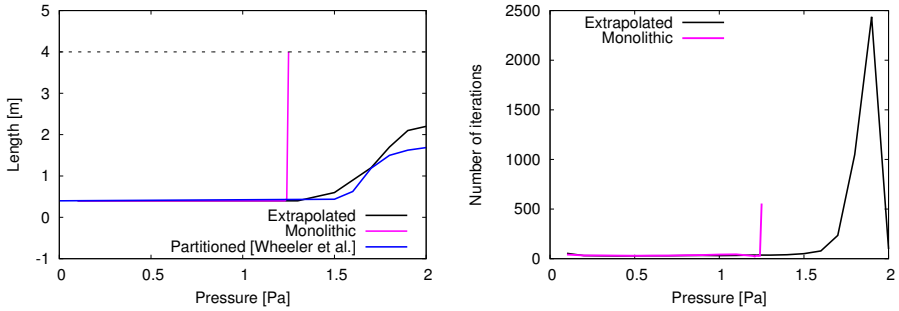

FIG. 5.12. *Example 4: Comparison of fracture length (at left) and number of Newton iterations per pressure step (at right). The maximal fracture length is bounded by the domain size, which is 4m. The fracture length is compared to the partitioned approach from Wheeler et al. [53].*

5.5. Screw tension tests. This fifth test is split into two subtests. In the first test, we will deal with crack nucleation due to high stresses, which demonstrates the claim that the phase-field model indeed recognizes high stress regions in which the material will damage. In the second test, an initial fracture is prescribed representing a hollow-rolled screw motivated by experimental data [54]. Here the final fracture pattern will be different than before resulting in branching, joining and a fracture network. The results are new in the sense that in [54] a staggered solution algorithm was adopted and we now tackle the problem with our quasi-monolithic (i.e., fully monolithic) approaches yielding unexpected findings.

Configuration. The geometric setting is displayed in Figure 5.13. The total length is $17.20mm$. The initial mesh is once uniformly refined yielding 13760 mesh elements. In Example 5a, the initial screw is undamaged. In Example 5b, an initial crack with the help of the phase-field variable is prescribed along $\Omega_F = \{x = 0 \pm 2h; -10mm \leq y \leq -7mm\}$.

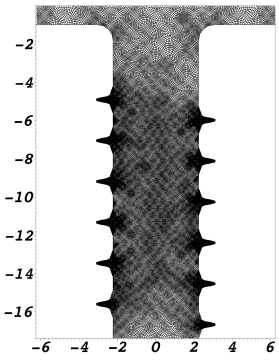

FIG. 5.13. *Example 5: Mesh of screw simulations. The screw is fixed at the bottom, at top we have non-homogeneous Dirichlet conditions in y-direction (uniform tension). The units are in mm.*

Boundary conditions. Crack growth is driven by a non-homogeneous Dirichlet condition for the displacement field u on Γ_{top}, the head of the screw at $y = 0.0$. We increase the displacement on Γ_{top} at each time step such that the head is pulled, namely

$$u_y = \delta t \times \bar{u}, \quad \bar{u} = 1.0 \text{ mm},$$

where $\delta t = 10^{-2}$s.

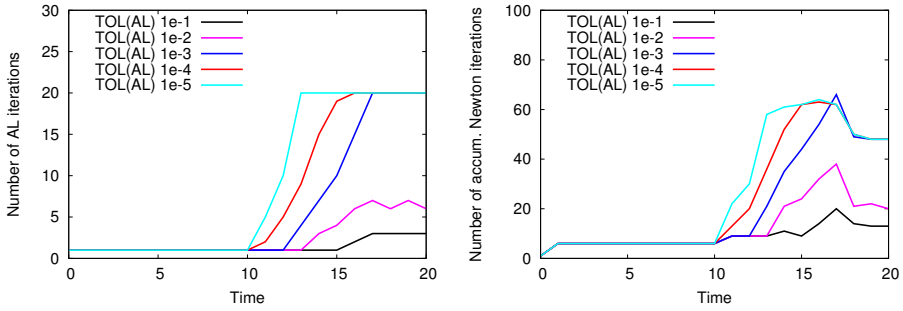

FIG. 5.14. *Example 5a: Number of augmented Lagrangian iterations per time step (left) and number of accumulated Newton iterations per time step (right).*

Parameters. As model parameters, we choose $\gamma = 1$, $\kappa = 10^{-10}h, \epsilon = 2h$ mm. We notice that the maximum number of possible augmented Lagrangian iterations is 20 and TOL_{AL} is variable as shown below. The Newton tolerance is $TOL_N = 10^{-8}$ in one set of tests. In a second series we adaptively determine TOL_N as explained

in Section 4.2. The total time in Example 5a (undamaged) is $T = 20s$ and in Example 5b (hollow-rolled) $T = 18s$ and the time step size is $\delta = 0.01s$. Actually the screw will be damaged earlier around $T = 15s$ but for the sake of a fair CPU time measuring we always compute until the final time. As material parameters, we use $\mu = 80.77kN/mm^2$, $\lambda = 121.15kN/mm^2$ and $G_c = 2.7N/mm$.

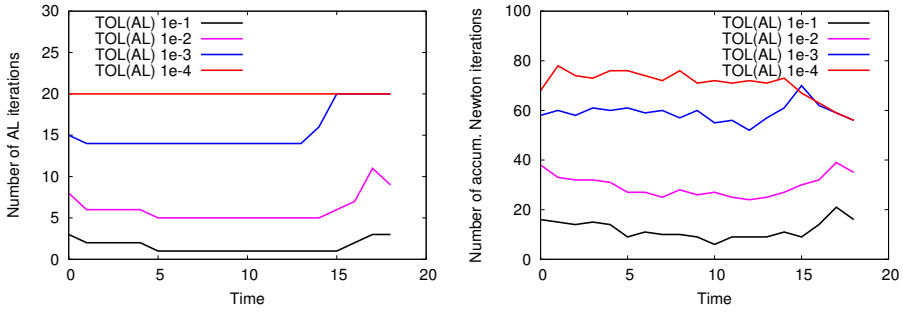

FIG. 5.15. *Example 5b: Number of augmented Lagrangian iterations per time step (left) and number of accumulated Newton iterations per time step (right). To obtain the average number of Newton iterations per augmented Lagrangian iteration per time step, one has to compute* $\frac{\#Newton}{\#augmentedLagrangian}$.

Quantities of interest. In this test, mesh refinement is not our purpose since we have studied this in great detail before. Rather:

- We observe the bulk energy

$$E_B = \int_\Omega ([1-\kappa]\varphi^2 + \kappa)\psi(e)\,dx, \tag{5.5}$$

  and the crack energy

$$E_C = \frac{G_c}{2}\int_\Omega \Big(\frac{(\varphi-1)^2}{\varepsilon} + \varepsilon|\nabla\varphi|^2\Big)\,dx, \tag{5.6}$$

  with the strain energy functional

$$\psi(e) := \mu \mathrm{tr}(e(u)^2) + \frac{1}{2}\lambda \mathrm{tr}(e(u))^2, \quad \text{with } e := e(u) := \frac{1}{2}(\nabla u + \nabla u^T),$$

  and $|\nabla\varphi|^2 := \nabla\varphi : \nabla\varphi$.
- Next we show visually that the crack (Example 5a) will really develop in the region with the highest stresses.
- Moreover we provide numbers for the Newton and augmented Lagrangian iterations, respectively, and numbers to assemble the Jacobian matrix, right hand side residual, and linear solves as well as CPU times using an Intel(R) Core(TM) i5-3320M CPU 2.60GHz machine.
- Additionally, we compare a fixed Newton tolerance with the inexact scheme.
- Then we vary the augmented Lagrangian tolerance, because this is actually the most expensive operation when the penalty parameters needs to be modified. This variation is studied with regard to the precision of certain quantities of interest as well as the computational cost.
- Finally in Example 5b, we also study when the augmented Lagrangian tolerance is too low, the crack will vanish and we recover the result from Example 5a.

Discussion of findings. We first observed that in these tests we are not able to work with the fully monolithic scheme. Independently of using the residual-based or error-oriented Newton scheme, the Newton solver will from the very first time steps not converge. Consequently, all presented results are obtained with the quasi-monolithic approach. Here both Newton schemes do converge and yield very satisfactory iteration numbers. The iteration numbers of the augmented Lagrangian and Newton schemes are presented in Figure 5.14 and 5.15. As goal functionals we compute the bulk and the crack energies as displayed in Figure 5.17. These goal functionals as well as the computational cost shown in Table 5.1 and 5.2 are studied with respect to the tolerance of the augmented Lagrangian scheme. The key interest is to understand the importance of a high precision of the penalization parameter with respect to other quantities. Indeed for Example 5a, we see from $TOL_{AL} = 1e-2$ (and lower) there is no change in the precision of the goal functional (and also the crack pattern - not shown here though) but significant higher computational cost. Thus, to achieve satisfying results at low computational cost there is no need to work with very low TOL_{AL}. These results are very similar to Example 5b. Here however the initial crack will vanish if TOL_{AL} is too large as shown in Figure 5.20. Reliable results of the crack pattern and stresses are provided in Figure 5.16, 5.18, 5.19. Finally we also see in Table 5.1 and 5.2 that the inexact scheme proposed in Proposition 4.2 significantly reduces the computational cost (up to 60% of the CPU times) while keeping the same precision for the goal functional values.

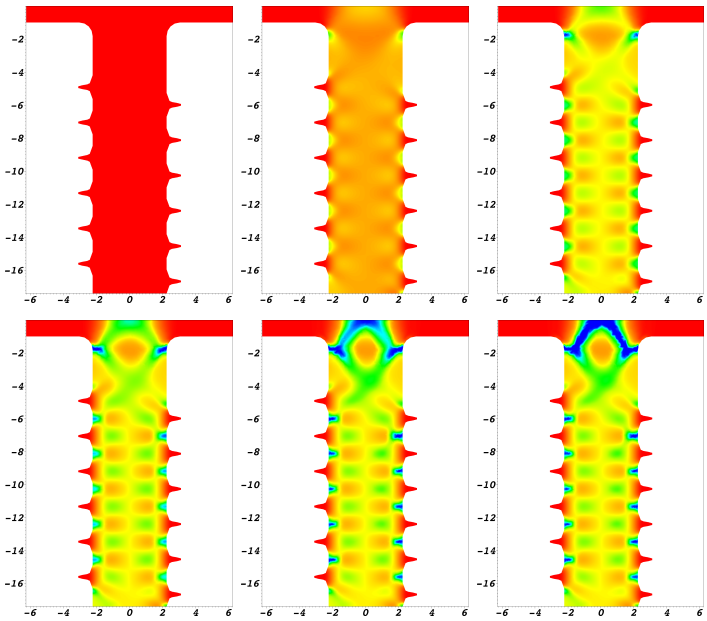

FIG. 5.16. *Example 5a: display of the phase-field variable at* $T = 0.01, 0.012, 0.015, 0.016, 0.017, 0.018s$. *Here two fractures develop at* $T = 0.015s$ *and at* $T = 0.018s$ *the entire head is broken. These results are in agreement with the findings in [54].*

TABLE 5.1

Example 5a: undamaged initial screw. Computational cost with respect to the augmented Lagrangian tolerance. The scheme 'Fixed' means that the Newton tolerance is fixed and 'inexact' denotes the inexact scheme in which the Newton tolerance is chosen as suggested in Proposition 4.2.

Scheme	TOL_{AL}	Assemble matrix	Assemble rhs	Solve linear sys.	CPU time
Fixed	$1e-1$	86	389	152	242s
Fixed	$1e-2$	112	556	213	334s
Fixed	$1e-3$	190	912	315	864s
Fixed	$1e-4$	222	1054	354	929s
Fixed	$1e-5$	247	1156	380	990s
Inexact	$1e-2$	83	348	123	220s
Inexact	$1e-3$	133	550	175	337s
Inexact	$1e-4$	172	696	216	413s

TABLE 5.2

Example 5b: hollow-rolled screw. Computational cost with respect to the augmented Lagrangian tolerance. The scheme 'Fixed' means that the Newton tolerance is fixed and 'inexact' denotes the inexact scheme in which the Newton tolerance is chosen as suggested in Proposition 4.2.

Scheme	TOL_{AL}	Assemble matrix	Assemble rhs	Solve linear sys.	CPU time
Fixed	$1e-1$	109	479	197	295s
Fixed	$1e-2$	221	1144	448	1103s
Fixed	$1e-3$	420	2268	829	1894s
Fixed	$1e-4$	509	2703	962	2124s
Inexact	$1e-2$	163	658	204	421s
Inexact	$1e-3$	351	1398	393	950s
Inexact	$1e-4$	434	1751	486	1140s

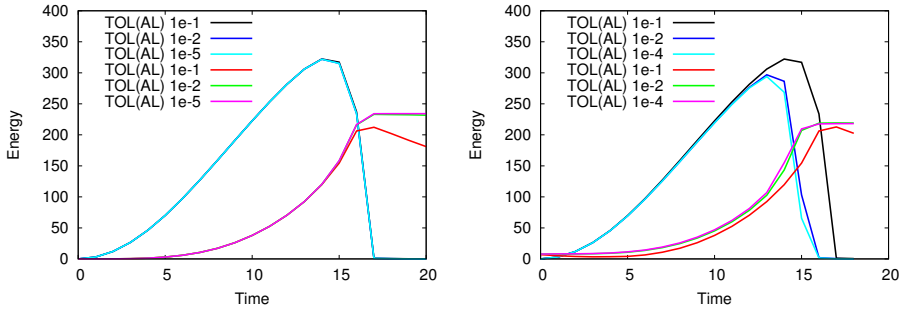

FIG. 5.17. *Example 5a/b: Bulk and crack energies for Example 5a and 5b, respectively. When the screw starts damaging at $T = 15s$ and $T = 13s$, respectively, we have (as expected) a sudden decrease of the bulk energy. After total damage the bulk energy remains zero and the crack energy neither changes anymore for all reliable tolerances $TOL_{AL} \leq 1e-2$.*

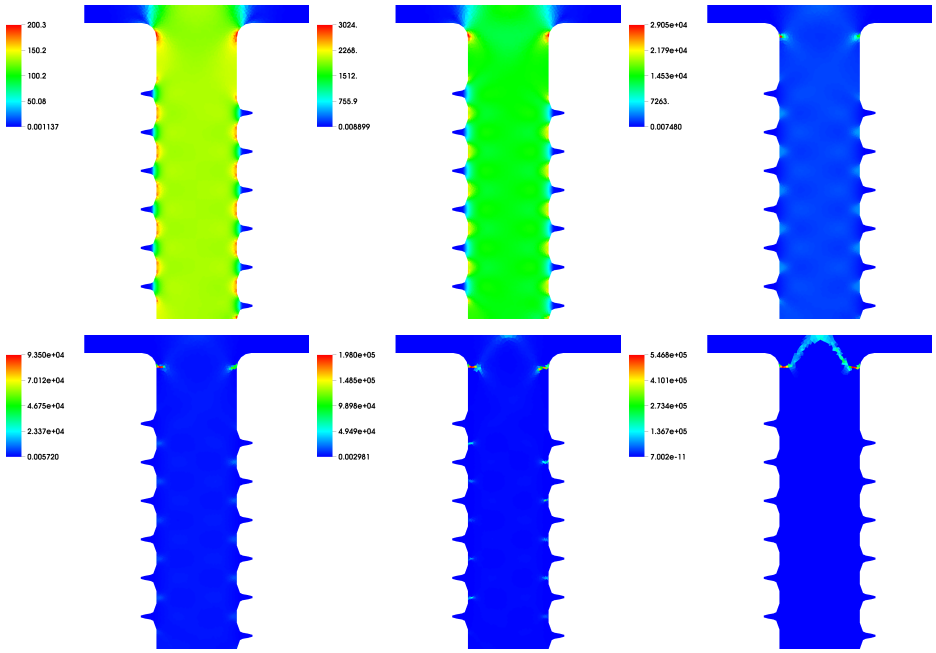

FIG. 5.18. *Example 5a: display of the stresses at* $T = 0.01, 0.012, 0.015, 0.016, 0.0170.0, 18s$. *Observing the stress evolution and the phase-field pattern in Figure 5.16, we see that two fractures nucleate in the regions with the highest stresses.*

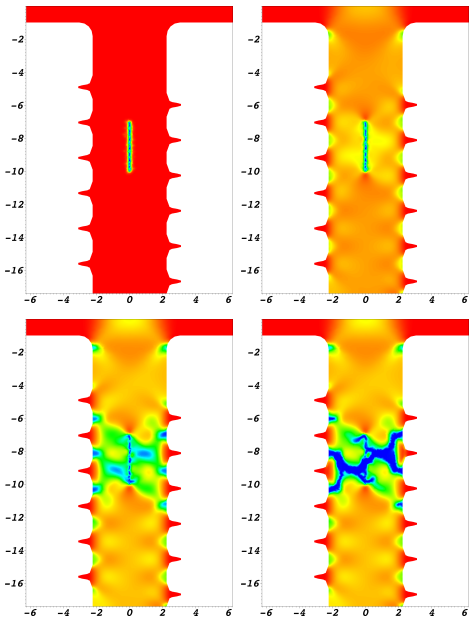

FIG. 5.19. *Example 5b: display of the crack pattern at* $T = 0.01, 0.012, 0.015, 0.017s$. *Here* $TOL_{AL} = 1e-4$ *is sufficiently small. The reader is referred to Figure 5.20 for a setting in which* TOL_{AL} *is not appropriate.*

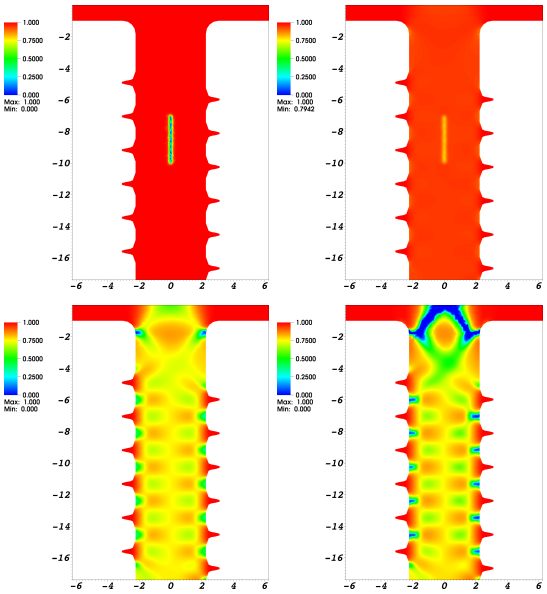

FIG. 5.20. *Example 5b: display of the crack pattern at* $T = 0.01, 0.07, 0.08, 0.015s$. *Here* $TOL_{AL} = 1e-1$ *is too low (and thus not reliable) and the initial crack pattern will vanish around* $T = 0.08s$. *Afterwards the configuration is the same as in Example 5a in which the screw will crack around the head. This test shows that in the case of an initial fracture, prescribed with phase-field, the tolerance* TOL_{AL} *must be sufficiently small.*

5.6. 3D testing: two pressurized fractures. In this final example we extend to 3D. The programming code is exactly the same as before and only requires to change one number in the programming code since the spatial dimension is a template parameter as usually done in deal.II. Since the computational cost is immediately high, we implemented local mesh refinement. We consider two initial fractures which are subject to increasing pressure such that they first join and later branch. Branching is due to the fact that we work in a heterogeneous material. This 3D configuration is inspired by the 2D example presented in [30].

Configuration. We work in the cube $B = (0, 10)^3$. Two initial fractures are located at $\Omega_{F1} = \{x = 2.6 \pm h; 3.8 \leq y \leq 5.5; z = 4 \pm h\}$ and $\Omega_{F2} = \{5.5 \leq x \leq 7; y = 4 \pm h; z = 6 \pm h\}$. The initial geometry is two times uniformly refined and three times locally in the subcube $B_{sub} = (3, 7)^3$. This yields 8576 mesh elements and 40364 degrees of freedom. The smallest h is $h_{min} = 0.54m$.

Parameters. The time step size is $\delta t = 1s$ and we compute until the fracture reaches the outer boundaries. Young's modulus is $E \in [2, 10]Pa$ (heterogeneous material) and Poisson's ratio is $\nu_s = 0.2$. Furthermore $G_c = 1.0N/m$. Moreover, $\gamma = 100$ and $\kappa = 10^{-10}h, \epsilon = 2h_{min}$. The pressure is linearly increasing (similar to Example 4):

$$p(t) = 0.001 + t \cdot 0.25.$$

Quantities of interest. In this example, we observe the fracture pattern, and compare again the quasi-monolithic and the fully monolithic scheme in terms of Newton iterations.

Discussion of findings. In this final example we highlight features of phase-field modeling in 3D as displayed in the Figures 5.22, 5.21, and 5.23. Therein we observe

that the two fractures will first grow, then join and later branch (see Figure 5.22). Branching is observed at several places, which is emphasized in a top view sequence in Figure 5.21. With regard to our algorithms a nice performance of the Newton solver is observed using the quasi-monolithic scheme with in average 28 accumulated Newton iterations per time step and 3 augmented Lagrangian iterations. Thus, per augmented Lagrangian iteration, we have about 10 Newton iterations. For the fully monolithic scheme we have to admit that the Newton performance was poor (45 accumulated Newton steps, i.e., 15 per augmented Lagrangian step and in addition the lower Newton tolerance was not always achieved). On the other hand, as in Example 4, the coupling conditions are tighter since fracture growth takes place at an earlier time in comparison to the quasi-monolithic scheme (namely $T = 8s$ in comparison to $T - 10s$; see Figures 5.22 and 5.23). Moreover, fracture growth is more brutally (since in Figure 5.23 from $T = 7s$ to $T = 8s$ the entire half plane is cracked). In summary, this example nicely illustrates various promising features of phase-field, but definitely needs more investigation from the algorithmic point of view when working with a fully monolithic scheme. On the other hand the quasi-monolithic approach yields satisfactory results from the numerical point of view.

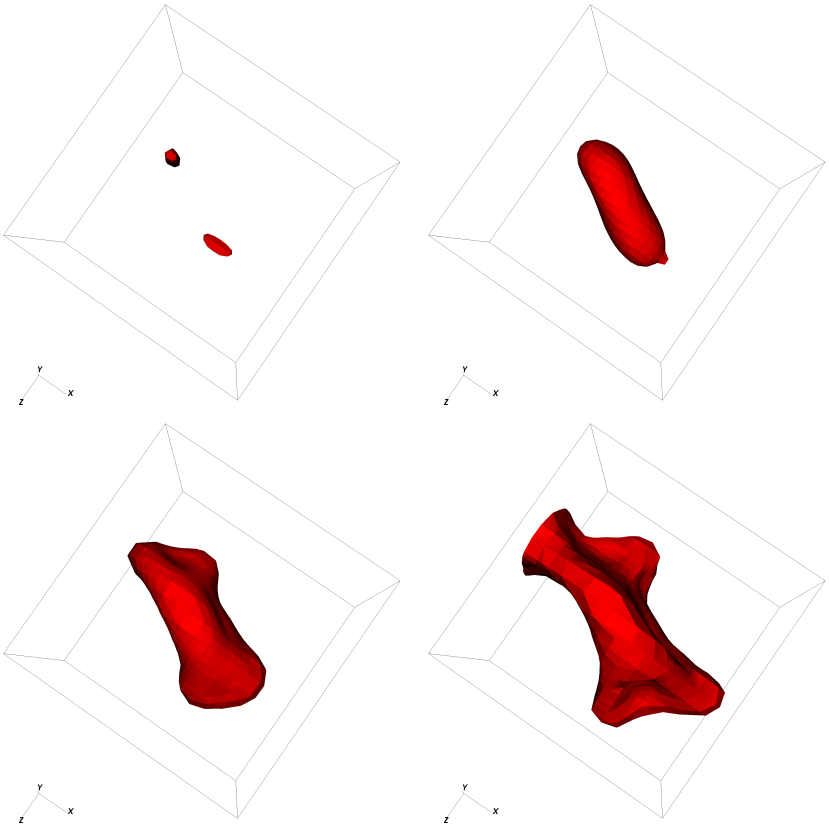

FIG. 5.21. *Example 6, top view: Fracture pattern at* $T = 1, 11, 13, 15s$. *Here we highlight the nonplanar fracture pattern and two regions where the fractures split.*

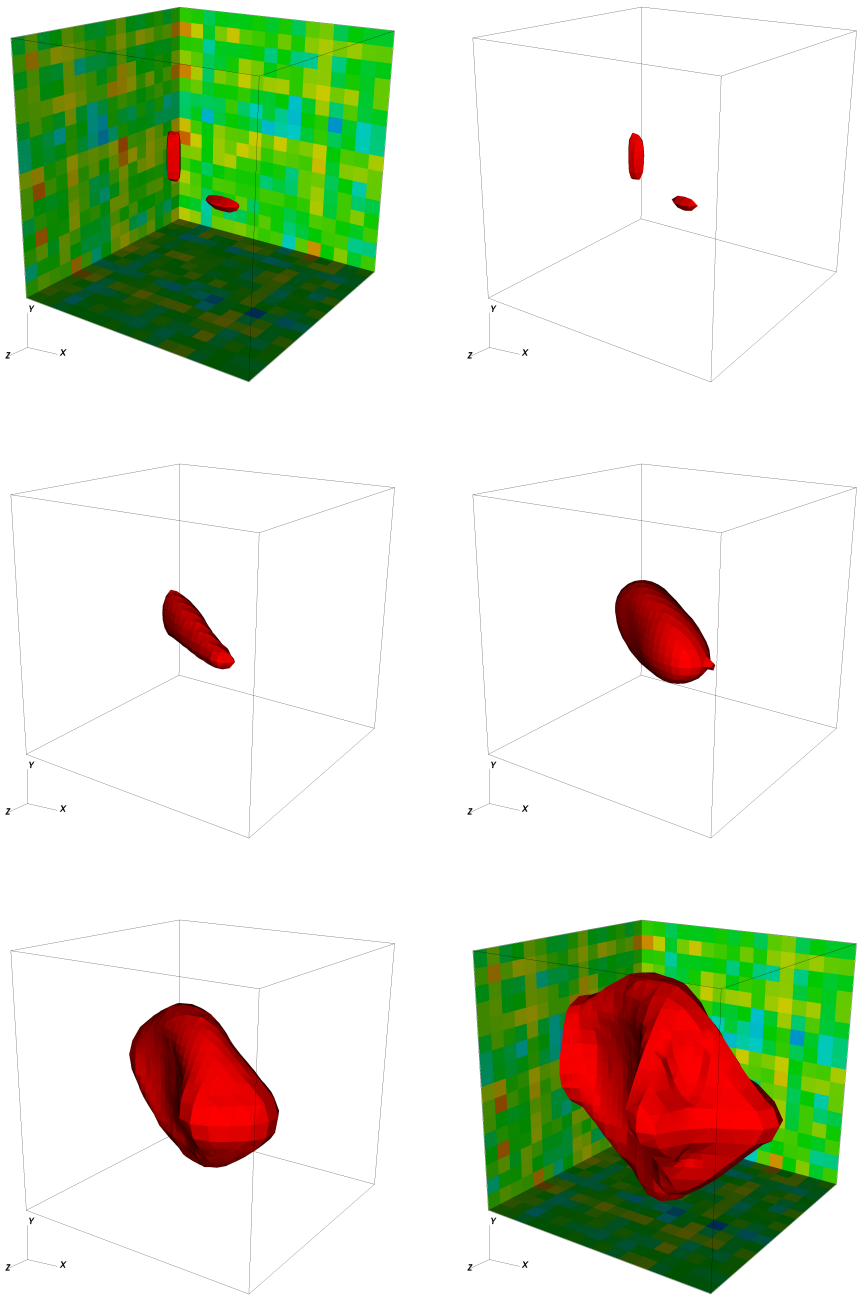

FIG. 5.22. *Example 6, side view: Fracture pattern at* $T = 1, 9, 10, 11, 13, 15s$. *The two fractures first grow, then join, and later split. In the first and last figure the nonhomogeneous material field (Young's modulus) is displayed.*

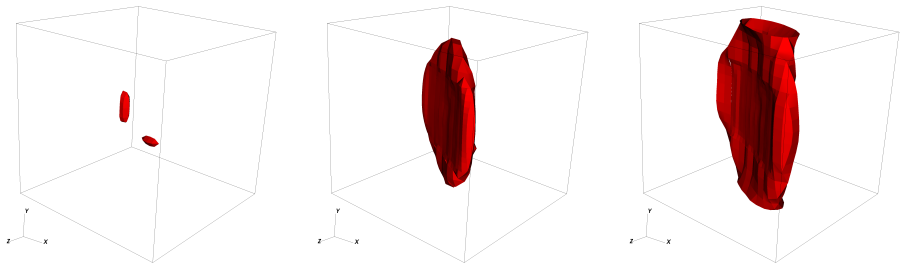

FIG. 5.23. *Example 6 (fully monolithic): Fracture pattern at $T = 7, 8, 9s$. Here the fracture pattern is different. More importantly this figure shows again that the coupling conditions are more tight when using the fully coupled scheme since the joining takes place much earlier (at $T = 8s$) in contrast to $T = 10s$ using the quasi-monolithic scheme.*

6. Concluding remarks and final discussion of the computational findings. In this work, an error-oriented Newton algorithm has been applied to phase-field fracture propagation problems. As already known from the literature this algorithm can cope with ill-conditioned nonlinear partial differential equations. In combination with the augmented Lagrangian iteration, we were indeed able to observe a better performance (in most examples) for nonlinear coupled phase-field fracture propagation problems. The Newton stopping criterion is adaptively chosen with respect to the error of the outer augmented Lagrangian loop, which is employed to enforce crack irreversibility. These ingredients allowed us to design a monolithic algorithm, which is a major advancement in achieving numerical stability, consistent Galerkin-based a posteriori error estimation and derivative-based optimization. Indeed the suggested error-oriented Newton method is robust and shows excellent behavior for two mechanics tests and a stationary pressurized fracture. For a propagating pressurized fracture, the performance (efficiency) should be improved in the future. Moreover, we also found that the differences between the quasi-monolithic extrapolated scheme and the new fully monolithic scheme depend on the setting. In the Examples 2 and 3, no significant differences with respect to goal-functional evaluations could be detected. In the other Examples 1 and 4, there are however (major) discrepancies. In Example 5 and 6 (3D) we studied more features of the phase-field model itself, namely nucleation, branching, joining and fracture networks. Our findings indicate that the extrapolated scheme performs much better than the fully monolithic approach. Secondly, if an initial fracture is prescribed with the help of phase-field (Example 5a) rather than in the initial mesh (Example 1), we need a certain tolerance of the augmented Lagrangian approach in order to ensure $\varphi = 0$ in the crack. However this tolerance does not need to be too tight. Several simulations substantiate these results. Moreover, the inexact augmented Lagrangian scheme yields a significant reduction in the computational cost. Finally in Example 6, a 3D example in a heterogeneous material is considered. Again, the extrapolated scheme performs much better and in addition the example is designed in such a way that two initial fractures will first join and later branch, which underlines the capabilities of the phase-field approach. But clearly, the last example should be computed with a parallel algorithm (as developed in [30, 33]) and adaptive mesh refinement since the computational cost is rather high. We leave this implementation as future work and notice that programming of mesh adaptivity is already on the way in current work.

Acknowledgments. I want to thank my former host institution RICAM Linz since half of the work has been carried out there. Furthermore I want to thank the referees for their positive evaluation of the first version with just very few and motivating comments, which however significantly improved the content of this paper resulting in the Examples 5 and 6.

REFERENCES

[1] G. Allaire, F. Jouve, and N. Van Goethem, *Damage and fracture evolution in brittle materials by shape optimization methods*, Journal of Computational Physics, 230 (2011), pp. 5010 – 5044.

[2] St. Almi, G. Dal Maso, and R. Toader, *Quasi-static crack growth in hydraulic fracture*, Nonlinear Analysis, 109 (2014), pp. 301–318.

[3] M. Ambati, T. Gerasimov, and L. De Lorenzis, *A review on phase-field models of brittle fracture and a new fast hybrid formulation*, Computational Mechanics, 55 (2015), pp. 383–405.

[4] L. Ambrosio and V.M. Tortorelli, *Approximation of functionals depending on jumps by elliptic functionals via γ-convergence*, Comm. Pure Appl. Math., 43 (1990), pp. 999–1036.

[5] ———, *On the approximation of free discontinuity problems*, Boll. Un. Mat. Ital. B, 6 (1992), pp. 105–123.

[6] H. Amor, J.-J. Marigo, and C. Maurini, *Regularized formulation of the variational brittle fracture with unilateral contact: Numerical experiments*, J. Mech. Phys. Solids, 57 (2009), pp. 1209–1229.

[7] M. Artina, M. Fornasier, S. Micheletti, and S. Perotto, *Anisotropic mesh adaptation for crack detection in brittle materials*, SIAM J. Sci. Comput., 37 (2015), pp. B633–B659.

[8] W. Bangerth, R. Hartmann, and G. Kanschat, *deal.II – a general purpose object oriented finite element library*, ACM Trans. Math. Softw., 33 (2007), pp. 24/1–24/27.

[9] W. Bangerth, T. Heister, and G. Kanschat, *Differential Equations Analysis Library*, 2012.

[10] R. Becker, D. Meidner, and B. Vexler, *Efficient numerical solution of parabolic optimization problems by finite element methods*, Optim. Methods Softw., 22 (2007), pp. 813–833.

[11] R. Becker and R. Rannacher, *An optimal control approach to error control and mesh adaptation in finite element methods*, Acta Numerica 2001, Cambridge University Press, a. iserles ed., 2001, pp. 1–102.

[12] M. J. Borden, C. V. Verhoosel, M. A Scott, T. J. R. Hughes, and C. M. Landis, *A phase-field description of dynamic brittle fracture*, Comput. Meth. Appl. Mech. Engrg., 217 (2012), pp. 77–95.

[13] B. Bourdin, *Numerical implementation of the variational formulation for quasi-static brittle fracture*, Interfaces and free boundaries, 9 (2007), pp. 411–430.

[14] B. Bourdin, G.A. Francfort, and J.-J. Marigo, *Numerical experiments in revisited brittle fracture*, J. Mech. Phys. Solids, 48 (2000), pp. 797–826.

[15] ———, *The variational approach to fracture*, J. Elasticity, 91 (2008), pp. 1–148.

[16] B. Bourdin, J.-J. Marigo, C. Maurini, and P. Sicsic, *Morphogenesis and propagation of complex cracks induced by thermal shocks*, Phys. Rev. Lett., 112 (2014), p. 014301.

[17] S. Burke, Ch. Ortner, and E. Süli, *An adaptive finite element approximation of a variational model of brittle fracture*, SIAM J. Numer. Anal., 48 (2010), pp. 980–1012.

[18] ———, *An adaptive finite element approximation of a generalized Ambrosio-Tortorelli functional*, M3AS, 23 (2013), pp. 1663–1697.

[19] X.-C. Cai and D. E. Keyes, *Nonlinearly preconditioned inexact newton algorithms*, SIAM Journal on Scientific Computing, 24 (2002), pp. 183–200.

[20] T. A. Davis and I. S. Duff, *An unsymmetric-pattern multifrontal method for sparse LU factorization*, SIAM J. Matrix Anal. Appl., 18 (1997), pp. 140–158.

[21] R.S. Dembo, S.C. Eisenstat, and T. Steihaug, *Inexact newton methods*, SIAM J. Numer. Anal., 19 (1982), pp. 400–408.

[22] P. Deuflhard, *Newton Methods for Nonlinear Problems*, vol. 35 of Springer Series in Computational Mathematics, Springer Berlin Heidelberg, 2011.

[23] M. Fortin and R. Glowinski, *Augmented Lagrangian Methods: Applications to the Numerical Solution of Boundary Value Problems*, Stud. Math. Appl. 15, North Holland, Amsterdam, 1983.

[24] G.A. Francfort and J.-J. Marigo, *Revisiting brittle fracture as an energy minimization problem*, J. Mech. Phys. Solids, 46 (1998), pp. 1319–1342.

[25] T. Gerasimov and L. De Lorenzis, *A line search assisted monolithic approach for phase-field computing of brittle fracture*, Computer Methods in Applied Mechanics and Engineering, 312 (2016), pp. 276 – 303. Phase Field Approaches to Fracture.

[26] T. Gerasimov and T. Wick, *Load-displacement curves for the L-shaped panel test.* Personal Correspondance at the 3rd phase-field GAMM conference in Braunschweig (Germany), Feb 2016.

[27] R. Glowinski and P. Le Tallec, *Augmented Lagrangian and Operator-Splitting Methods in Nonlinear Mechanics*, SIAM Stud. Appl. Math. 9, SIAM, Philadelphia, 1989.

[28] A. A. Griffith, *The phenomena of rupture and flow in solids.*, Philos. Trans. R. Soc. Lond., 221 (1921), pp. 163–198.

[29] Y. Heider and B. Markert, *A phase-field modeling approach of hydraulic fracture in saturated porous media*, Mechanics Research Communications, (2016), pp. –.

[30] T. Heister, M. F. Wheeler, and T. Wick, *A primal-dual active set method and predictor-corrector mesh adaptivity for computing fracture propagation using a phase-field approach*, Comp. Meth. Appl. Mech. Engrg., 290 (2015), pp. 466 – 495.

[31] M. R. Hestenes, *Multiplier and gradient methods*, J. Optim. Theory Appl., 4 (1969), pp. 303–320.

[32] C. Kuhn and R. Müller, *A new finite element technique for a phase field model of brittle fracture*, Journal of Theoretical and Applied Mechanics, 49 (2011), pp. 1115–1133.

[33] S. Lee, M. F. Wheeler, and T. Wick, *Pressure and fluid-driven fracture propagation in porous media using an adaptive finite element phase field model*, Computer Methods in Applied Mechanics and Engineering, 305 (2016), pp. 111 – 132.

[34] ———, *Iterative coupling of flow, geomechanics and adaptive phase-field fracture including level-set crack width approaches*, Journal of Computational and Applied Mathematics, 314 (2017), pp. 40 – 60.

[35] S. Lee, M. F. Wheeler, T. Wick, and S. Srinivasan, *Initialization of phase-field fracture propagation in porous media using probability maps of fracture networks.*, Mechanics Research Communications, (2016), pp. –.

[36] A. Mesgarnejad, B. Bourdin, and M.M. Khonsari, *Validation simulations for the variational approach to fracture*, Computer Methods in Applied Mechanics and Engineering, 290 (2015), pp. 420 – 437.

[37] C. Miehe, M. Hofacker, L.-M. Schaenzel, and F. Aldakheel, *Phase field modeling of fracture in multi-physics problems. part ii. coupled brittle-to-ductile failure criteria and crack propagation in thermo-elasticplastic solids*, Computer Methods in Applied Mechanics and Engineering, 294 (2015), pp. 486 – 522.

[38] C. Miehe, M. Hofacker, and F. Welschinger, *A phase field model for rate-independent crack propagation: Robust algorithmic implementation based on operator splits*, Comput. Meth. Appl. Mech. Engrg., 199 (2010), pp. 2765–2778.

[39] C. Miehe and S. Mauthe, *Phase field modeling of fracture in multi-physics problems. part iii. crack driving forces in hydro-poro-elasticity and hydraulic fracturing of fluid-saturated porous media*, Computer Methods in Applied Mechanics and Engineering, (2015), pp. –.

[40] C. Miehe, L.-M. Schaenzel, and H. Ulmer, *Phase field modeling of fracture in multi-physics problems. part i. balance of crack surface and failure criteria for brittle crack propagation in thermo-elastic solids*, Computer Methods in Applied Mechanics and Engineering, 294 (2015), pp. 449 – 485.

[41] C. Miehe, F. Welschinger, and M. Hofacker, *Thermodynamically consistent phase-field models of fracture: variational principles and multi-field fe implementations*, Int. J. Numer. Methods Engrg., 83 (2010), pp. 1273–1311.

[42] A. Mikelić, M.F. Wheeler, and T. Wick, *A phase-field approach to the fluid filled fracture surrounded by a poroelastic medium.* ICES Report 13-15, Jun 2013.

[43] A. Mikelić, M. F. Wheeler, and T. Wick, *A phase-field method for propagating fluid-filled fractures coupled to a surrounding porous medium*, SIAM Multiscale Model. Simul., 13 (2015), pp. 367–398.

[44] A. Mikelić, M. F. Wheeler, and T. Wick, *Phase-field modeling of a fluid-driven fracture in a poroelastic medium*, Computational Geosciences, 19 (2015), pp. 1171–1195.

[45] A. Mikelić, M. F. Wheeler, and T. Wick, *A quasi-static phase-field approach to pressurized fractures*, Nonlinearity, 28 (2015), pp. 1371–1399.

[46] J. Nocedal and S. J. Wright, *Numerical optimization*, Springer Ser. Oper. Res. Financial Engrg., 2006.

[47] G. Pillo, G. Liuzzi, S. Lucidi, and L. Palagi, *A truncated newton method in an augmented lagrangian framework for nonlinear programming*, Computational Optimization and Applications, 45 (2008), pp. 311–352.

[48] M. J. D. Powell, *A method for nonlinear constraints in minimization problems*, in Optimization (Sympos., Univ. Keele, Keele, 1968), Academic Press, 1969, pp. 283–298.
[49] A. Schlüter, A. Willenbücher, Ch. Kuhn, and R. Müller, *Phase field approximation of dynamic brittle fracture*, Comput. Mech., 54 (2014), pp. 1141–1161.
[50] I. N. Sneddon, *The distribution of stress in the neighbourhood of a crack in an elastic solid*, Proc. R Soc London A, 187 (1946), pp. 229–260.
[51] I. N. Sneddon and M. Lowengrub, *Crack problems in the classical theory of elasticity*, SIAM series in Applied Mathematics, John Wiley and Sons, Philadelphia, 1969.
[52] J. Vignollet, S. May, R. Borst, and C. V. Verhoosel, *Phase-field models for brittle and cohesive fracture*, Meccanica, 49 (2014), pp. 2587–2601.
[53] M.F. Wheeler, T. Wick, and W. Wollner, *An augmented-Lagangrian method for the phase-field approach for pressurized fractures*, Comp. Meth. Appl. Mech. Engrg., 271 (2014), pp. 69–85.
[54] D. Wick, T. Wick, H. R. Hellmig, and H.-J. Christ, *Numerical simulations of crack propagation in screws with phase-field modeling*, Computational Materials Science, 109 (2015), pp. 367–379.
[55] T. Wick, *Coupling fluid-structure interaction with phase-field fracture*, Journal of Computational Physics, 327 (2016), pp. 67 – 96.
[56] ———, *Goal functional evaluations for phase-field fracture using PU-based DWR mesh adaptivity*, Computational Mechanics, 57 (2016), pp. 1017–1035.
[57] B.J. Winkler, *Traglastuntersuchungen von unbewehrten und bewehrten Betonstrukturen auf der Grundlage eines objektiven Werkstoffgesetzes fuer Beton*, PhD thesis, University of Innsbruck, 2001.